Highlights

Deep neural network method for predicting the iron concentration in silicon solar cell by current-voltage characteristic

Oleg Olikh,Oleg Lozitsky,Oleksii Zavhorodnii

- Proposed deep learning-based method to predict iron contamination in Si-SC by using IV curve.

- The simulated IV characteristics is used to create training and test datasets.

- The mean squared relative error of prediction is up to 0.005.

Deep neural network method for predicting the iron concentration in silicon solar cell by current-voltage characteristic

Oleg Olikh[a,*], Oleg Lozitsky[a] and Oleksii Zavhorodnii[a]

[a]*Taras Shevchenko National University of Kyiv, 64/13, Volodymyrska Street, City of Kyiv, Ukraine, 01601*

ARTICLE INFO

Keywords:
Ideality factor
Silicon
n^+-p-p^+ structure
SCAPS
Iron contamination
Machine learning

ABSTRACT

Defect-assisted recombination processes frequently limit the photovoltaic device performance. The low-cost and express methods of impurity contamination control are in demand at solar cell manufacturing. In this paper, we used deep learning-based approach to extract the iron concentration in silicon solar cell from an ideality factor values. We used SCAPS-1D to simulate solar cell with the back surface field design and to generate labeled training and test datasets. Our results showed the deep neural network ability to predict iron concentration with mean squared relative error up to 0.005 by using ideality factor values, SC base thickness and doping level, and temperature. The simulation shows that the prediction error is reduced for high doping level, low temperature, and using of two ideality factor value (for structure with interstitial iron atoms only as well as for for structure with coexistence of Fe_i and iron-boron pair).

1. Introduction

Metal contamination control remains an important challenge for silicon processing both for microelectronics, logic technologies and solar cells (SCs) [1, 2, 3, 4]. Typically, metal related defect characterization is performed by Fourier-transform infrared spectroscopy, electron-paramagnetic resonance, minority carrier lifetime measurements, deep level transient spectroscopy (DLTS), Laplace DLTS etc [5, 6, 7]. However, these techniques are time-consuming, require special equipment or/and sample preparing. At the same time, the current-voltage (IV) measurement is a standard rapid industrial SC characterization technique. IV characteristics contain important information about electrically active defects [6, 8]. And a few defect diagnostics by IV characteristics are proposed [6, 8, 9, 10, 11]. The temperature dependencies of current components [10, 11] or IV differential parameters [8, 9] are under consideration. But the numerous and high accuracy IV measurements are required in the first and second cases, respectively.

In our previous work [12], we have shown that the SC ideality factor value (n) can be used to estimate the iron concentration (N_{Fe}). It should be noted that the ideality factor is quite often used to characterize the various semiconductor barrier structures [13, 14, 15, 16, 17]. However, a defect's signature in an ideality factor is convoluted with those from so many other physical processes. As a result the obtained analytic expressions $N_{Fe} = f(n)$ are not general and the numerous grading curves are needed to N_{Fe} determination; besides the IV measurements over a temperature range are necessary [12]. On the other hand, in the last decade, the deep learning, which is enable to solve problems without clear algorithmization, have been successfully used in various fields of theoretical and applied physics [18, 19, 20]. Furthermore, materials informatics (combination of material property calculations/measurements and informatics algorithms) has been asserted [21] to become the fourth (along with theory, simulations, and experiments) paradigm of science. The aim of this work is to apply the deep learning approach for predicting the iron concentration from ideality factor (so to say "deep learning for deep levels"). Further, unlike in previous work [12], the back surface field (BSF) n^+-p-p^+ structure was under consideration and the base thickness influence on ideality factor was taken into account as well.

As the approximation to the practical using, the paper considers a fairly simple system which consists of crystalline silicon (c-Si) SC and iron impurity. However, the system is important in practice. Silicon solar cells constitute 90% of current global production capacity [22] and BSF is one of popular designs used for industrial mass production of c-Si SCs [23]. Iron is a major as one of the most detrimental metal impurities in c-Si SCs [2, 3, 4]. The flowchart of the used heuristic approach is shown in Fig. 1. The following milestones can be distinguished. First, the dark IV characteristic

---

*Corresponding author

✉ olegolikh@knu.ua (Oleg Olikh)
ORCID(s):
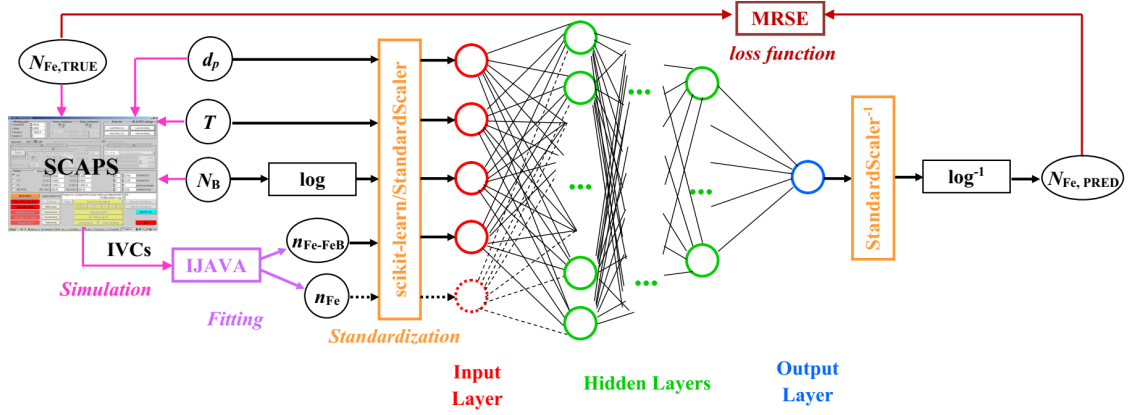
Figure 1: Schematic of deep learning based approach for predicting the iron concentration. Additional details are discussed in the body of the article.

is simulated for SCs with both known contaminant composition and various parameters. In our numerical simulation we make use of SCAPS-1D [24, 25], which widely used to model silicon-based devices [26, 27, 28]. Second, the obtained characteristic is fitted according to the double-diode model and the ideality factor is estimated. As a result of aforesaid steps, the labeled datasets were produced. Obviously, the labeled dataset from experimental IVs would be preferable, but it is practically difficult to find the thousands of samples with the required parameters. Third, the training of deep neural network (DNN) to estimate an iron contamination by using SC's base thickness, doping level, temperature, and ideality factor value. Fours, the DNN testing.

2. Simulation Details

The presented calculation uses n^+–p–p^+ structure. n^+ is the emitter layer with the donor concentration $N_D = 10^{19}$ cm^{-3} and the thickness 0.5 μm. p and p^+ are the base and BSF-layer, respectively, which are uniformly doped with boron. 1 μm and 5×10^{18} cm^{-3} are the thickness d_{BSF} and the acceptor concentration N_{BSF} of the p^+ layer. The base with the thickness $d_p = 150$–240 μm is doped with concentration $N_B = 10^{15}$–10^{17} cm^{-3}.

The simulations were carried out over the temperature range $290 - 340$ K. The SCAPS setting file was created for each temperature using the following material parameters. The bandgap E_G and bandgap narrowing ΔE_G models are, respectively, from Pässler [29] and Yan and Cuevas [30]:

$$E_G = E_{G0} - \alpha\Theta\left\{\frac{1-3\Delta^2}{e^{\frac{\Theta}{T}}-1} + \frac{3\Delta^2}{2}\left(\sqrt[6]{1 + \frac{\pi^2}{3(1+\Delta^2)}\left(\frac{2T}{\Theta}\right)^2 + \frac{3\Delta^2-1}{4}\left(\frac{2T}{\Theta}\right)^3 + \frac{8}{3}\left(\frac{2T}{\Theta}\right)^4 + \left(\frac{2T}{\Theta}\right)^6} - 1\right)\right\}, \quad (1)$$

$$\Delta E_G = 4.20 \times 10^{-5}\left[\ln\left(\frac{N_D}{10^{14}}\right)\right]^3 ; \qquad \Delta E_G = 4.72 \times 10^{-5}\left[\ln\left(\frac{N_{B,BSF}}{10^{14}}\right)\right]^3, \quad (2)$$

where $E_{G0} = 1.1701$ eV, $\alpha = 3.23 \times 10^{-4}$ eV/K, $\Theta = 446$ K, $\Delta = 0.51$. The carrier thermal velocities are calculated from models by Green [31]:

$$v_{\text{th},n} = \sqrt{\frac{8qkT}{0.28m_0\pi}} ; \qquad v_{\text{th},p} = \sqrt{\frac{8qkT}{0.41m_0\pi}}, \quad (3)$$

where m_0 is the free electron mass. The effective states density masses in the conduction band m^*_{dC} and the valence band m^*_{dV} are calculated according to models from Couderc et al. [32]:

$$\left(\frac{m^*_{dC}}{m_0}\right)^{1.5} = 1.094 - 1.312 \times 10^{-5}T + 6.753 \times 10^{-7}T^2 + 4.609 \times 10^{-10}T^3, \quad (4)$$

$$\left(\frac{m_{dV}^*}{m_0}\right)^{1.5} = 0.3426 + 3.376 \times 10^{-3}T - 4.689 \times 10^{-6}T^2 + 2.525 \times 10^{-9}T^3 . \tag{5}$$

The carrier mobilities and the free carrier effective masses are from Klaassen [33] and O'Mara et al. [34], respectively. The temperature and doping dependencies of Auger recombination coefficients are calculated from models by Altermatt et al. [35]:

$$\begin{aligned}
C_p(T) = & (7.91 \times 10^{-32} - 4.13 \times 10^{-35}T + 3.59 \times 10^{-37}T^2) \\
& \times \left(1 + \left(564812 T^{-1.6545} - 1 \right) \left(1 - \tanh \left[\left\{ \frac{p}{5 \times 10^{16}} \right\}^{0.29} \right] \right) \right),
\end{aligned} \tag{6}$$

$$C_n(T) = 2.8 \times 10^{-31} \times \left(1 + \left(235548 T^{-1.5013} - 1 \right) \left(1 - \tanh \left[\left\{ \frac{n}{5 \times 10^{16}} \right\}^{0.34} \right] \right) \right). \tag{7}$$

The Auger recombination coefficient is from Nguyen et al. [36].

The outside surface recombination with electron and hole velocities 10^3 cm/s was taken into account.

The simulations are carried out under the assumption that the defect–assisted recombination is connected with iron–related deep levels only. As the base and the SBF-layer uniform contaminant, iron is assumed to be in concentration $N_{Fe} = 10^{10}$–10^{13} cm^{-3}. The simulations have been performed for the following two cases. In the first one, the concentration of totally dissolved iron is given by a sum of the concentration of the interstitial iron Fe_i and the concentration of trigonal iron-boron pair Fe_iB_s:

$$N_{Fe} = N_{Fe_i} + N_{Fe_iB_s} . \tag{8}$$

The defect distributions are uniform, depend on the Fermi level F position, and are given by [37, 38]:

$$\frac{N_{FeB}}{N_{Fe}} = \frac{N_B 10^{-23} \exp\left(-\frac{E_b}{kT}\right)}{\left[1 + \frac{N_B}{10^{23}} \exp\left(-\frac{E_b}{kT}\right)\right] \left[1 + \exp\left(-\frac{F - E_{Fe_i}}{kT}\right)\right]} , \quad N_{Fe_i} = N_{Fe} - N_{FeB} , \tag{9}$$

where $E_b = 0.582$ eV is the binding energy of the Fe_iB_s pairs, E_{Fe_i} is the donor level, associated with Fe_i. This case correspond to the equilibrium condition and is labeled "Fe-FeB" from now on.

In the second one, the Fe_i is suggested to be only present with uniform distribution ($N_{Fe_i} = N_{Fe}$). This case can be realized by heat treatment (210°C, 3 min) [39] or intense illumination [40] and is referred as "Fe-FeB" hereafter.

The donor level $E_{Fe_i} = E_V + 0.394$ eV with electron $\sigma_{n,Fe} = 3.47 \times 10^{-11} T^{-1.48}$ cm^2 and hole $\sigma_{p,Fe} = 4.54 \times 10^{-16} \exp\left(-\frac{0.05}{kT}\right)$ cm^2 capture cross-sections [37, 41] is associated with Fe_i in simulations. The donor level $E_{FeB}^D = E_V + 0.10$ eV, $\sigma_{n,FeB}^D = 4 \times 10^{-13}$ cm^2, $\sigma_{p,FeB}^D = 2 \times 10^{-14}$ cm^2 and acceptor level $E_{FeB}^A = E_C - 0.26$ eV, $\sigma_{n,FeB}^A = 5.1 \times 10^{-9} T^{-2.5}$ cm^2, $\sigma_{p,FeB}^A = 3.32 \times 10^{-10} \exp\left(-\frac{0.262}{kT}\right)$ cm^2 [42, 37, 41] are used for Fe_iB_s.

The dark forward IV characteristic were generated by SCAPS over a voltage range up to 0.45 V. According to the two-diode model, the dark SC current is given by [43]

$$I = I_{01} \left[\exp\left(-\frac{q(V - R_s I)}{kT}\right) - 1 \right] + I_{02} \left[\exp\left(-\frac{q(V - R_s I)}{nkT}\right) - 1 \right] + \frac{V - R_s I}{R_{sh}} , \tag{10}$$

where I_{01} and I_{02} are the saturation currents, R_{sh} and R_s are the shunt and series resistances. The two-diode model are often used to describe real Si SCs and we used Eq. 10 to fit the simulated data by taking n, I_{01}, I_{02}, R_{sh}, and R_s as fitting parameters. The fitting was performed by using the meta–heuristic method IJAVA [44]. It should be noted that influence of both R_s (obtained values < 10^{-2} Ω) and R_{sh} (obtained values > 10^{18} Ω) can be neglected in simulated IV.

It is the ideality factor value n which is used in our further calculation. The ideality factors, which are obtained in Fe-case and Fe-FeB-case, are referred as n_{Fe} and n_{Fe-FeB} hereafter. The typical simulated dependencies of the ideality factor are shown in Fig. 2. The detailed discussion about n_{Fe} and n_{Fe-FeB} values are presented elsewhere [45], however it should be noted that (i) n can takes equal values for different SC parameters values; (ii) dependencies of n_{Fe} and n_{Fe-FeB} varies slightly.
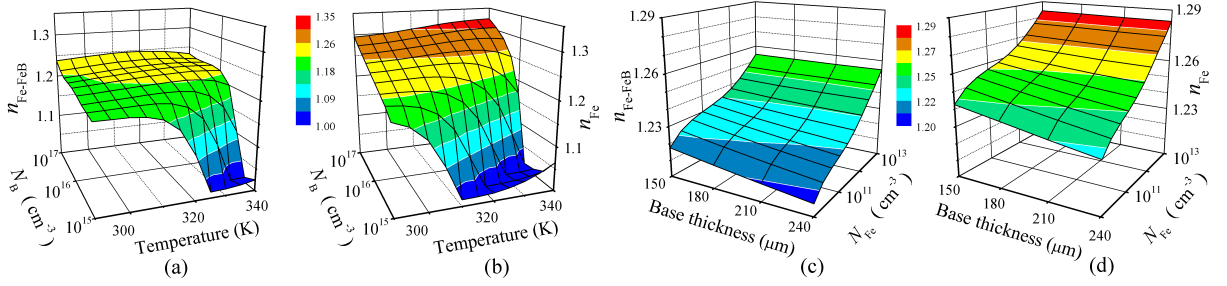
Figure 2: Ideality factor versus temperature and boron concentration (a, b) or base thickness and iron concentration (c,d). The Fe-FeB-case (a, c) and Fe-case (b, d). $N_{\text{Fe}} = 10^{10}$ cm^{-3} (a,b), $d_p = 180$ μm (a, b), $N_{\text{B}} = 10^{16}$ cm^{-3} (c, d), $T = 320$ K (c, d).

3. Deep neural network models

Training a deep neural network requires a large number of samples. In order to build a training dataset, we used IV characteristics, which are simulated by using 4 d_p values, 9 N_{B} values, 11 T values and 19 N_{Fe} values. These base thickness, doping level, temperature, and iron concentration values are regularly (for T and d_p in linear scale, for N_{Fe} and N_{B} in logarithmic scale) distributed over the ranges 150–240 μm, 10^{15}–10^{17} cm^{-3}, $290 - 340$ K, and 10^{10}–10^{13} cm^{-3}, respectively. Thus, 7524 IV characteristics are simulated in Fe-case as well as in Fe-FeB-case to to build a training dataset.

Besides, several test datasets are prepared. The d_p, N_{B}, and N_{Fe} values, which equal to values from training dataset, and T values, which is divergent from training dataset, are used to build the test dataset, labeled "T-varied". These dataset is based on 894 pairs of IV characteristics. The similar approach was used to prepare "d-varied" (1189 samples), "Fe-varied" (856 samples), and "B-varied" (514 samples) test datasets. The base thickness, doping level, temperature, and iron concentration values, which are divergent from training dataset values, are used to prepare "All-varied" (684 samples).

The precise parameters values are listed in Supplementary Material.

We have tried to construct the DNN, which is able to estimate iron contamination by using SC parameters (d_p and N_{B}), measurement temperature, and result of IV fitting (ideality factor value). As it is shown in Fig. 1 two DNNs with different input parameters were under consideration. The input sample of the first one consist of $\{d_p, \log N_{\text{B}}, T, n_{\text{Fe-FeB}}\}$. In practice, these input set can be obtained from one dark IV measurement. These neural network referred as DNN$_{\text{FeFeB}}$ hereafter. The second one uses $\{d_p, \log N_{\text{B}}, T, n_{\text{Fe-FeB}}, n_{\text{Fe}}\}$ in input layer. In practice, the obtaining of such a set requires additional SC processing (e.g. intense illumination) and two IV measuring. The label DNN$_{\text{FeFeB-Fe}}$ is used below.

The dense deep neural network was implemented through the high-level Keras API provided by TensorFlow [46]. The input layers consist of 4 or 5 nodes — see Fig. 1. 1 node and linear activation were used in output layer. The five configurations oh hidden layers were under consideration: (i) "pipe": each hidden layer contains equal number of nodes; (ii) "trapezium": six hidden layers, number of neural linearly decreases from 100% (first layer) to 50% (last layer); (iii) "triangle": ten layers, number of neural linearly decreases from 100% (first layer) to 10% (last layer); (iv) "butterfly": two serial reflected trapezium configurations; (v) "fir": two serial trapezium configurations.

The loss function was chosen mean squared relative error (MSRE):

$$\text{MSRE} = \frac{1}{N_s} \sum_{i=1}^{N_s} \frac{(N_{\text{Fe,TRUE,i}} - N_{\text{Fe,PRED,i}})^2}{N_{\text{Fe,TRUE,i}} \cdot N_{\text{Fe,PRED,i}}}, \tag{11}$$

where N_s is the number of samples in dataset, $N_{\text{Fe,TRUE,i}}$ is the iron concentration, which was used in simulation of i–th sample, $N_{\text{Fe,PRED,i}}$ is the DNN prediction for i–th sample.

Hyperparameters include the number of nodes for first hidden layer, the number of hidden layers (in pipe configuration), the batch size, the activation function, the optimizer, the learning rate, the preprocessing method, the dropout rate, the regularization function, the regularization rate, and the weight initializer. A grid search (coarse tuning to limit one hyperparameter) and random search (fine tuning) were performed over the predefined hyperparameter space,

shown in Table 1, and the best hyperparameter combination is chosen.

Table 1
Hyperparameter space for DNNs.

Hyperparameter	Values
# nodes for first hidden layer	30, 40, 50, 75, 100, 120, 150
# hidden layers	4, 5, 6, 8, 10, 15
batch size	8, 16, 32, 64, 128
activation function	ReLu, sigmoid, tanh, SELU, ELU
optimizer	SGD, RMSprop, Adam, Adadelta, Adagrad, Adamax, Nadam, Ftrl
learning rate	10^{-5}, 10^{-4}, 10^{-3}, 10^{-2}
epoch	100, 300, 400, 600, 1000, 1500
preprocessing method	StandartScaler, MinMaxScaler
regularization function	None, L2, L1, Dropout
regularization rate	10^{-5}, 10^{-4}, 10^{-3}, 10^{-2}
dropout rate	0.2, 0.3, 0.4, 0.5
weight initializer	Xavier Normal or Uniform, He Normal or Uniform, Random Normal or Uniform, Ones

10–fold cross–validation was used to estimate DNN training. The MSRE, coefficient of determination R^2, and coefficient of correlation R were three metrics used to evaluate the performance of the DNN models on test datasets. Finally, in order to increase a DNNs performance, the full dataset, which consists of training dataset and all test datasets, was used to train models.

4. Results and discussion

The results of hyperparameter search are listed in Table 2. In particular, the trapezium and pipe configurations are chosen for DNN_{FeFeB} and $DNN_{FeFeB-Fe}$ respectively.

Table 2
Chosen hyperparameter combinations.

Hyperparameter	DNN_{FeFeB}	$DNN_{FeFeB-Fe}$
# nodes for hidden layers	120, 108, 96, 84, 72, 60	100, 100, 100, 100
batch size	32	32
activation function	ReLu	ELU
optimizer	Adamax	Adamax
learning rate	10^{-3}	10^{-3}
epoch	400	1500
preprocessing method	StandartScaler	StandartScaler
regularization function	None	None
weight initializer	Xavier Normal	Xavier Normal

The training and test results of DNN_{FeFeB} are presented in Table 3, Table 4, and Fig. 3. One can see, that MSRE of DNN_{FeFeB} prediction is sufficiently great. But it should be noted, that the fraction of prediction with a great difference between $N_{Fe,TRUE,i}$ and $N_{Fe,PRED,i}$ is not big in most cases. Thus squared relative error (SRE) does not exceed 0.05 for 87%, 88%, and 96% samples from T-varied, d-varied and Fe-varid datasets respectively — see bars in Fig. 3. For B-varied dataset (with doping level value, which unused in training dataset) the biggest MSRE = 1.06 connects to occurrence of some samples with a really big SRE (>20). While SRE is less than 0.05 in 54% of samples from B-varied test dataset. The worst predictions is quite expectedly to have observed for the All-varied dataset: R^2 equals to 0.813 and SRE is less than 0.05 for 18% only. On the other hand, the Fe-varied dataset is most similar to real demand. And determination and correlation coefficients are high enough (0.991 and 0.996) in this case.

The dependencies on DNN prediction error on SC parameters values are under consideration too — see Figs. 4– 7. These figures represent data for training dataset, the results for test datasets are quite similar. Thus Fig. 4(a) shows that

Table 3
Results of 10–fold cross–validation

Dataset	MSRE	
	DNN_{FeFeB}	$DNN_{FeFeB-Fe}$
training	0.31 ± 0.07	0.03 ± 0.01
full	0.28 ± 0.05	0.03 ± 0.01

Table 4
DNN's testing results

Dataset	DNN_{FeFeB}			$DNN_{FeFeB-Fe}$		
	MSRE	R^2	R	MSRE	R^2	R
T–varied	0.41	0.936	0.967	0.020	0.994	0.997
d–varied	0.37	0.961	0.980	0.018	0.996	0.998
B–varied	1.06	0.881	0.939	0.084	0.991	0.995
Fe–varied	0.06	0.991	0.996	0.005	0.999	0.999
All–varied	0.54	0.813	0.901	0.138	0.948	0.974
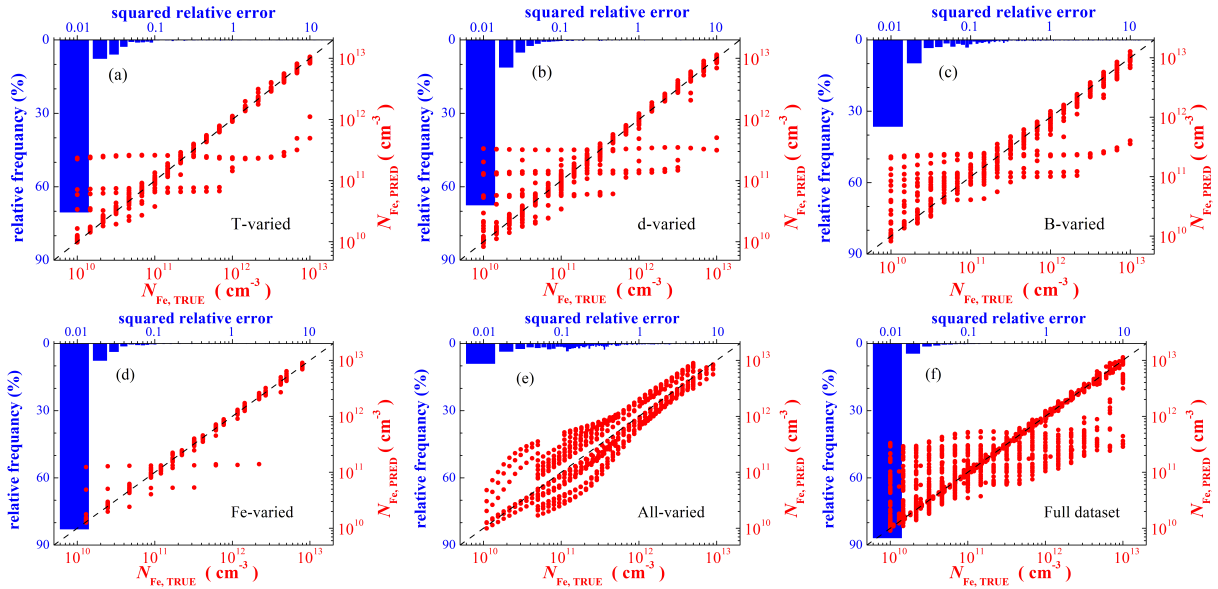
Figure 3: Iron concentrations are plotted against those generated by DNN_{FeFeB} on T-varied (a), d-varied (b), B-varied (c), Fe-varied (d), All-varied (e), and full (f) datasets (red points). Bars represent histograms of squared relative error. DNN was learned by training (a)–(e) or full (f) dataset. The black dashed lines are the identify lines servings as the references.

the considerable increase in prediction error value is observed at $T > 320$ K for DNN_{FeFeB}. So the maximum SRE is about 20 and the SRE is less than 0.01 for 55% of samples at $T = 340$ K (Fig. 4(c)). Whereas those values are equal to 0.02 and 83% at $T = 290$ K (Fig. 4(b)). It has been shown previously [45], that temperature rise causes the increase in the intrinsic recombination's contribution to an ideality factor. As a result, the sign of Shockley-Read-Hall (SRH) recombination in n value become less evident and DNN predictive ability fallen.

As it is shown on Fig. 5, the SC base thickness does non influence on the prediction error (mean value as well as relative frequency) practically. But one can see in Fig 2(c,d), that an ideality factor value depend on base thickness at constant N_{Fe}. Therefore d_p is important parameters for DNN training.
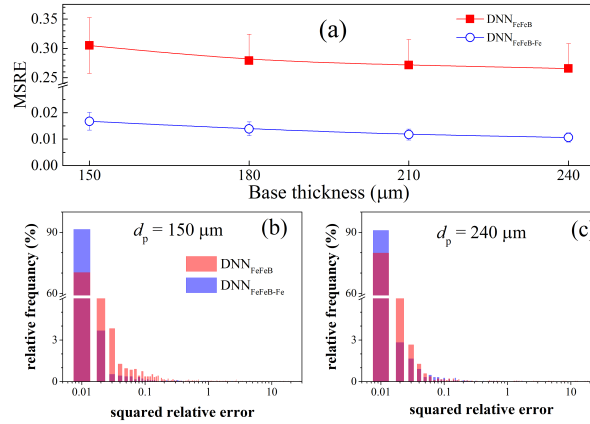
The predictive error rises sharply with doping level decrees — see Fig. 6(a). Thus maximum SRE is about 0.05 for $N_B = 10^{17}$ cm^{-3} (Fig. 6(c)) whereas squared relative error is less than 0.05 for 56% of samples only for
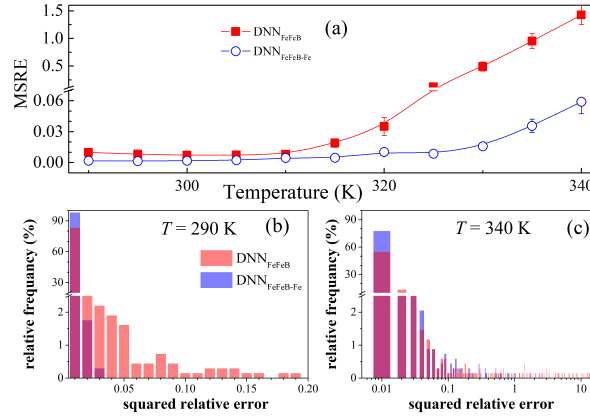
Figure 4: (a) Dependence of the MSRE (training dataset) on the temperature. (b),(c) Histograms of squared relative error for $T = 290$ K and $T = 340$ K. Red: DNN_{FeFeB}; blue: $DNN_{FeFeB-Fe}$.

Figure 5: (a) Dependence of the MSRE (training dataset) on the base thickness. (b),(c) Histograms of squared relative error for $d_p = 150$ μm and $d_p = 240$ μm. Red: DNN_{FeFeB}; blue: $DNN_{FeFeB-Fe}$.

$N_B = 10^{15}$ cm^{-3} (Fig. 6(b)). The hole occupation of the Fe-related level determines the SRH recombination efficiency. Accordingly to the Fermi-Dirac statistics, the probability of a hole occupation in a non-degenerate p-type semiconductor with full acceptor depletion can be expressed as

$$f_p = \frac{1}{1 + \frac{N_V}{N_B} \exp\left(\frac{E_V - E_{Fe_i}}{kT}\right)} .$$ (12)

If N_B decreases, the level is filled with an electron, the SRH recombination ceases, and the ideality factor value sharply reduces — Fig. 2(a,b). Besides, a weak influence of impurities on ideality factor under low doping condition is a reason of observed MSRE increase. In our opinion, the level filling is additional reason of an error increase at high temperature as well.

Fig. 7(a) shows that MSRE increases at both low and high iron concentrations. First N_{Fe} area of bad DNN accuracy is quite foreseeable, second one is surprising enough. But accordingly to Fig 7(c), the MSRE increasing at $N_{Fe} = 10^{13}$ cm^{-3} is most likely determined by a few samples with big SRE value. Whereas SRE increasing is more systematic at $N_{Fe} = 10^{13}$ cm^{-3} — Fig 7(b).

The ideality factor value for the the case of interstitial iron only presence (n_{Fe}) gives additional information about defects in comparing with n_{Fe-FeB}. It is not surprising that $DNN_{FeFeB-Fe}$ has better operating parameters in comparing with DNN_{FeFeB} — see Table 3, Table 4, Fig. 8. The operation improvement appearances in the MSRE decrease as well as in absence of huge difference between $N_{Fe,TRUE}$ and $N_{Fe,PRED}$ values and narrowing of SRE range (Figs. 4-8).
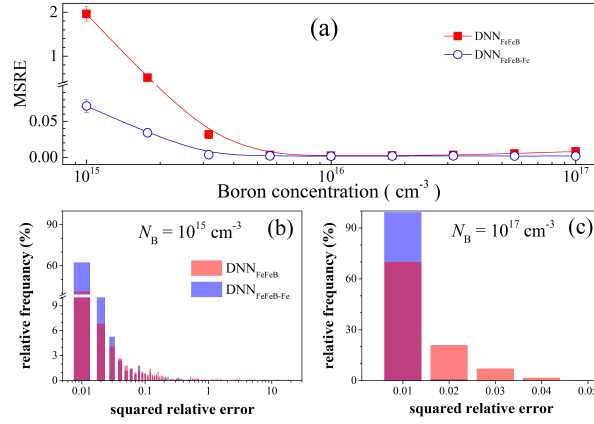
Figure 6: (a) Dependence of the MSRE (training dataset) on the boron concentration. (b),(c) Histograms of squared relative error for $N_B = 10^{15}$ cm^{-3} and $N_B = 10^{17}$ cm^{-3}. Red: DNN$_{FeFeB}$; blue: DNN$_{FeFeB-Fe}$.
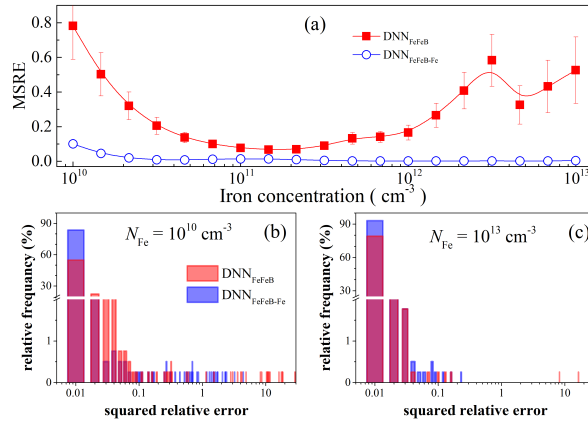
Figure 7: (a) Dependence of the MSRE (training dataset) on the iron concentration. (b),(c) Histograms of squared relative error for $N_{Fe} = 10^{10}$ cm^{-3} and $N_{Fe} = 10^{13}$ cm^{-3}. Red: DNN$_{FeFeB}$; blue: DNN$_{FeFeB-Fe}$.

Really, it is shown in Fig. 8 that the maximum SRE does not exceed 1 even in the case of All-varied datasets and SRE is less than 0.02 for 93%, 92%, 73%, and 97% of samples of T-varied, d-varied, B-varied, and Fe-varied datasets respectively. The R^2 (0.999) and R (0.999) values for Fe-varied dataset draws attention as well.

Despite the difference in predicting accuracy, DNN$_{FeFeB-Fe}$ features are similar to DNN$_{FeFeB}$ ones. Thus the DNN training with N_B values, which is expected in object of future research, is important for prediction accuracy (Fig. 8); the increase in the temperature value (Fig. 4) as well as decrease in doping level (Fig. 6) or iron concentration (Fig. 7) results in error rise. It should be noted that the prediction error gain with N_{Fe} increase not observed in DNN$_{FeFeB-Fe}$ case and SRE range at $N_{Fe} = 10^{13}$ cm^{-3} is more narrow then those at $N_{Fe} = 10^{10}$ cm^{-3} — see Fig. 7(b,c).

The results of training both DNN$_{FeFeB}$ and DNN$_{FeFeB-Fe}$ with full dataset are presented in Table 3, Fig. 3(f), and Fig. 8(f). One can see that the extension of labeled dataset does not practically improve DNN result in our case. In our opinion these is evidence of i) a good DNN configuration tuning; ii) a limited predictive ability of DNN$_{FeFeB}$, which caused by ambiguity of dependence $n_{Fe-FeB} = f(N_{Fe})$.

5. Conclusion and Outlook

In this paper, we extracted the iron concentration in silicon BSF solar cell from an ideality factor value and systematically studied the performance of deep learning in this problem. This is the first attempt to use deep learning for deep levels parameter retrieval from current-voltage curve. In this model study, we used simulation to obtain training
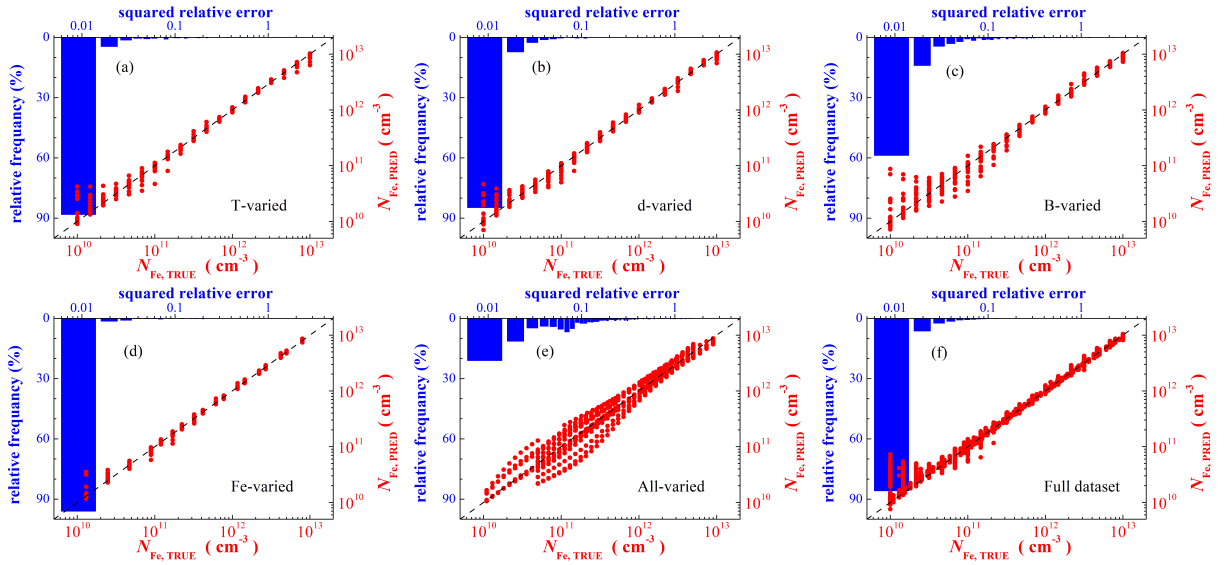
Figure 8: Iron concentrations are plotted against those generated by DNN$_{\text{FeFeB-Fe}}$ on T-varied (a), d-varied (b), B-varied (c), Fe-varied (d), All-varied (e), and full (f) datasets (red points). Bars represent histograms of squared relative error. DNN was learned by training (a)–(e) or full (f) dataset. The black dashed lines are the identify lines servings as the references.

and test labeled datasets. Our results showed the deep neural network ability to predict iron concentration with MSRE up to 0.005 by using ideality factor values, SC base thickness and doping level, and temperature. The simulation has shown that two ideality factor values (for structure with Fe$_i$ only as well as with Fe$_i$B$_s$ and Fe$_i$ coexistence) would be needed to substantially upgrade a prediction accuracy. It was important to train DNN with a boron concentration value, which agreed with doping level of investigated structures. Moreover the increase of iron concentration or boron concentration as well as temperature decrease results in a prediction error reducing.

The proposed approach envisages the utilization of a simple and widely applicable setup and does not require a much time. Therefore it could be integrated into manufacturing environment. However, it should be noted that we have simplified the task for our purposes. In our opinion there are two ways to further improve method. First one connects with an refining of labeled datasets and can be realized by using 3D-simulators (e.g. SILVACO TCAD) or an real IV measurements in a broad set of SCs. The improving of DNN operation is the second one and the fine-tuning is like most promising in this case. For example, a not numerous input parameters can be multiplied and transformed to the picture and apply a vision model (e.g. VGG16).

CRediT authorship contribution statement

Oleg Olikh: Conceptualization, Methodology, Formal analysis, Data Curation, Writing - Review & Editing, Visualization, Supervision. **Oleg Lozitsky:** Software, Validation, Investigation, Writing - Original Draft. **Oleksii Zavhorodnii:** Software, Validation, Formal analysis, Writing - Original Draft.

Data availability

The simulated IV characteristics, n_{Fe} and $n_{\text{Fe-FeB}}$ values, and trained DNNs are available at
https://github.com/olegolikh/IVcharacteristics.git.

Declaration of competing interest

The authors declare that they have no known competing financial interests or personal relationships that could have appeared to influence the work reported in this paper.

Acknowledgment

References

[1] C. Claeys, E. Simoen, Metal Impurities in Silicon- and Germanium-Based Technologies: Origin, Characterization, Control, and Device Impact, volume 270 of *Springer Series in Materials Science*, Springer International Publishing, Berlin/New York, 2018.

[2] H. Zhu, X. Yu, X. Zhu, Y. Wu, J. He, J. Vanhellemont, D. Yang, Low temperature iron gettering by grown-in defects in p–type Czochralski silicon, Superlattices Microstruct. 99 (2016) 192–196.

[3] J. Schmidt, Effect of dissociation of iron–boron pairs in crystalline silicon on solar cell properties, Progress in Photovoltaics: Research and Applications 13 (2005) 325–331.

[4] M. Schubert, M. Padilla, B. Michl, L. Mundt, J. Giesecke, J. Hohl-Ebinger, J. Benick, W. Warta, M. Tajima, A. Ogura, Iron related solar cell instability: Imaging analysis and impact on cell performance, Sol. Energy Mater. Sol. Cells 138 (2015) 96–101.

[5] D. K. Schroder, Semiconductor Material and Device Characterization, John Wiley & Sons, New Jersey, third edition, 2006.

[6] R. C. Kurchin, J. R. Poindexter, V. Vähänissi, H. Savin, C. del Cañizo, T. Buonassisi, How much physics is in a current-voltage curve? inferring defect properties from photovoltaic device measurements, IEEE J. Photovolt. 10 (2020) 1532–1537.

[7] A. R. Peaker, V. P. Markevich, J. Coutinho, Tutorial: Junction spectroscopy techniques and deep-level defects in semiconductors, J. Appl. Phys. 123 (2018) 161559.

[8] S. V. Bulyarskiy, A. V. Lakalin, M. A. Saurov, G. G. Gusarov, The effect of vacancy-impurity complexes in silicon on the current-voltage characteristics of p-n junctions, J. Appl. Phys. 128 (2020) 155702.

[9] S. V. Bulyarskiy, The effect of electron-phonon interaction on the formation of reverse currents of p-n-junctions of silicon-based power semiconductor devices, Solid-State Electron. 160 (2019) 107624.

[10] C. Claeys, E. Simoen, Device performance as a metrology tool to detect metals in silicon, physica status solidi (a) 216 (2019) 1900126.

[11] E. Simoen, C. Claeys, J. Vanhellemont, Defect analysis in semiconductor materials based on p-n junction diode characteristics, in: Defects and Diffusion in Semiconductors - An Annual Retrospective IX, volume 261 of *Defect and Diffusion Forum*, Trans Tech Publications Ltd, 2007, pp. 1–24.

[12] O. Olikh, Relationship between the ideality factor and the iron concentration in silicon solar cells, Superlattices Microstruct. 136 (2019) 106309.

[13] A. S. H. van der Heide, A. Schonecker, J. H. Bultman, W. C. Sinke, Explanation of high solar cell diode factors by nonuniform contact resistance, Progress in Photovoltaics: Research and Applications 13 (2005) 3–16.

[14] L. Duan, H. Yi, C. Xu, M. B. Upama, M. A. Mahmud, D. Wang, F. H. Shabab, A. Uddin, Relationship between the diode ideality factor and the carrier recombination resistance in organic solar cells, IEEE Journal of Photovoltaics 8 (2018) 1701–1709.

[15] J. Chen, M. Zhu, X. Lu, X. Zou, Electrical characterization of GaN Schottky barrier diode at cryogenic temperatures, Appl. Phys. Lett. 116 (2020) 062102.

[16] P. Dalapati, N. Manik, A. Basu, Analysis of the temperature dependence of diode ideality factor in InGaN-based UV-A light-emitting diode, Semiconductors 54 (2020) 1284–1289.

[17] P. Calado, D. Burkitt, J. Yao, J. Troughton, T. M. Watson, M. J. Carnie, A. M. Telford, B. C. O'Regan, J. Nelson, P. R. Barnes, Identifying dominant recombination mechanisms in perovskite solar cells by measuring the transient ideality factor, Phys. Rev. Applied 11 (2019) 044005.

[18] G. Carleo, I. Cirac, K. Cranmer, L. Daudet, M. Schuld, N. Tishby, L. Vogt-Maranto, L. Zdeborová, Machine learning and the physical sciences, Rev. Mod. Phys. 91 (2019) 045002.

[19] S. Ju, S. Shimizu, J. Shiomi, Designing thermal functional materials by coupling thermal transport calculations and machine learning, J. Appl. Phys. 128 (2020) 161102.

[20] S. Rodrigues, H. G. Ramos, F. Morgado-Dias, Machine learning pv system performance analyser, Prog. Photovoltaics Res. Appl. 26 (2018) 675–687.

[21] S. Ju, S. Shimizu, J. Shiomi, Designing thermal functional materials by coupling thermal transport calculations and machine learning, J. Appl. Phys. 128 (2020) 161102.

[22] J. Jean, P. R. Brown, R. L. Jaffe, T. Buonassisi, V. Bulović, Pathways for solar photovoltaics, Energy Environ Sci. 8 (2015) 1200–1219.

[23] J. Ajayan, D. Nirmal, P. Mohankumar, M. Saravanan, M. Jagadesh, L. Arivazhagan, A review of photovoltaic performance of organic/inorganic solar cells for future renewable and sustainable energy technologies, Superlattices Microstruct. 143 (2020) 106549.

[24] M. Burgelman, P. Nollet, S. Degrave, Modelling polycrystalline semiconductor solar cells, Thin Solid Films 361–362 (2000) 527–532.

[25] K. Decock, S. Khelifi, M. Burgelman, Modelling multivalent defects in thin film solar cells, Thin Solid Films 519 (2011) 7481–7484.

[26] E. Hu, G. Yue, R. Zhang, Y. Zheng, L. Chen, S. Wang, Numerical simulations of multilevel impurity photovoltaic effect in the sulfur doped crystalline silicon, Renewable Energy 77 (2015) 442–446.

[27] A. Hamache, N. Sengouga, A. Meftah, M. Henini, Modeling the effect of 1 MeV electron irradiation on the performance of n$^+$–p–p$^+$ silicon space solar cells, Radiat. Phys. Chem. 123 (2016) 103–108.

[28] K. Kim, J. Gwak, S. K. Ahn, Y.-J. Eo, J. H. Park, J.-S. Cho, M. G. Kang, H.-E. Song, J. H. Yun, Simulations of chalcopyrite/c-si tandem cells using scaps-1d, Sol. Energy 145 (2017) 52–58.

[29] R. Pässler, Dispersion-related description of temperature dependencies of band gaps in semiconductors, Phys. Rev. B 66 (2002) 085201.

[30] D. Yan, A. Cuevas, Empirical determination of the energy band gap narrowing in p$^+$ silicon heavily doped with boron, J. Appl. Phys. 116 (2014) 194505.

[31] M. A. Green, Intrinsic concentration, effective densities of states, and effective mass in silicon, J. Appl. Phys. 67 (1990) 2944–2954.

[32] R. Couderc, M. Amara, M. Lemiti, Reassessment of the intrinsic carrier density temperature dependence in crystalline silicon, J. Appl. Phys. 115 (2014) 093705.

[33] D. Klaassen, A unified mobility model for device simulation — I. model equations and concentration dependence, Solid-State Electron. 35 (1992) 953– 959.

[34] W. O'Mara, R. Herring, L. Hant, Handbook of semiconductor silicon technology, Noyes Publications, New Jersey, USA, 1990.

[35] P. P. Altermatt, J. Schmidt, G. Heiser, A. G. Aberle, Assessment and parameterisation of Coulomb–enhanced Auger recombination coefficients in lowly injected crystalline silicon, J. Appl. Phys. 82 (1997) 4938–4944.

[36] H. T. Nguyen, S. C. Baker-Finch, D. Macdonald, Temperature dependence of the radiative recombination coefficient in crystalline silicon from spectral photoluminescence, Appl. Phys. Lett. 104 (2014) 112105.

[37] J. D. Murphy, K. Bothe, M. Olmo, V. V. Voronkov, R. J. Falster, The effect of oxide precipitates on minority carrier lifetime in p–type silicon, J. Appl. Phys. 110 (2011) 053713.

[38] W. Wijaranakula, The reaction kinetics of iron–boron pair formation and dissociation in p–type silicon, J. Electrochem. Soc. 140 (1993) 275–281.

[39] G. Zoth, W. Bergholz, A fast, preperetion-free method to detect irpn in silicon, J. Appl. Phys. 67 (1990) 6764–6771.

[40] L. J. Geerligs, D. Macdonald, Dynamics of light-induced feb pair dissociation in crystalline silicon, Appl. Phys. Lett. 85 (2004) 5227–5229.

[41] F. E. Rougieux, C. Sun, D. Macdonald, Determining the charge states and capture mechanisms of defects in silicon through accurate recombination analyses: A review, Solar Energy Materials and Solar Cells 187 (2018) 263 – 272.

[42] A. A. Istratov, H. Hieslmair, E. Weber, Iron and its complexes in silicon, Applied Physics A: Materials Science & Processing 69 (1999) 13–44.

[43] O. Breitenstein, Understanding the current-voltage characteristics of industrial crystalline silicon solar cells by considering inhomogeneous current distributions, Opto–Electronics Review 21 (2013) 259–282.

[44] K. Yu, J. Liang, B. Qu, X. Chen, H. Wang, Parameters identification of photovoltaic models using an improved JAYA optimization algorithm, Energy Conversion and Management 150 (2017) 742–753.

[45] O. Y. Olikh, O. V. Zavhorodnii, Modeling of ideality factor value in n^+–p–p^+–si structure, Journal of Physical Studies 24 (2020) 4701.

[46] F. Chollet, Deep Learning with Python, Manning, second edition, 2017.